Energy & Environmental Science

Accepted Manuscript

This article can be cited before page numbers have been issued, to do this please use: T. Wang, J. Duan, B. Zhang, W. Luo, X. Ji, H. Xu, Y. Huang, L. Huang, Z. Song, J. Wen, C. Wang, Y. Huang and J. B. Goodenough, *Energy Environ. Sci.*, 2022, DOI: 10.1039/D1EE03604A.

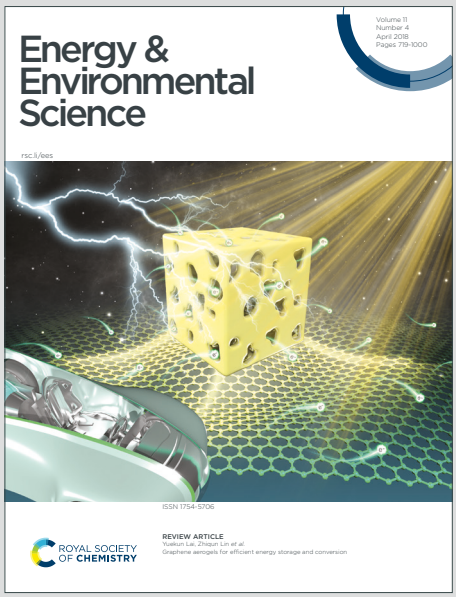

ROYAL SOCIETY OF CHEMISTRY

rsc.li/ees

View Article Online
DOI: 10.1039/D1EE03604A

A self-regulated gradient interphase for dendrite-free solid-state Li batteries

Authors: Tengrui Wang[1]†, Jian Duan[1]†, Bao Zhang[2]†, Wei Luo[1]*, Xiao Ji[2], Henghui Xu[3,4], Ying Huang[1], Liqiang Huang[1], Zhenyou Song[1], Jiayun Wen[1], Chunsheng Wang[2]*, Yunhui Huang[4]*, John B. Goodenough[3*]

[1]Institute of New Energy for Vehicles, School of Materials Science and Engineering, Tongji University, Shanghai 201804, China

[2]Department of Chemical & Biomolecular Engineering, University of Maryland College Park, College Park, Maryland, 20742, United States

[3]Materials Science and Engineering Program and Department of Mechanical Engineering, The University of Texas at Austin, Austin 78712 TX, USA.

[4]State Key Laboratory of Material Processing and Die & Mould Technology, School of Materials Science and Engineering, Huazhong University of Science and Technology, Wuhan 430074, China

* Corresponding authors: weiluo@tongji.edu.cn (W.L.); cswang@umd.edu (C.S.W.); jgoodenough@mail.utexas.edu (J.B.G.); huangyh@hust.edu.cn (Y.H.H)

Keywords: solid-state battery; gradient anode; kinetics; high current densities;

View Article Online
DOI: 10.1039/D1EE03604A

Abstract

Solid-state Li metal batteries (SSLMBs) have emerged as an important energy storage technology that offers the possibility of both high energy density and safety by combining a Li metal anode (LMA), a high-capacity cathode and a nonflammable solid-state electrolyte (SSE). However, the major challenges of poor LMA/SSE interface wetting and the easy growth of Li dendrites in SSEs remain unsolved. Here, we have addressed these challenges by using a functional gradient Li anode (FGLA), which is formed through a self-regulated reaction between molten Li and AlF_3. A composition gradient of Li-LiAl-LiF is spontaneously formed from the reaction of molten Li with AlF_3 due to the large difference of interfacial energy between Li/LiAl and Li/LiF, where the LiAl reduces the interface resistance and LiF suppresses Li dendrites. The FGLA not only dramatically reduces the resistance at FGLA/$Li_{6.5}La_3Zr_{1.5}Ta_{0.5}O_{12}$ (LLZTO) garnet SSE interface to ~1 $\Omega \cdot cm^2$, but also largely increases the critical current density (CCD) to over 3.0 $mA \cdot cm^{-2}$ at room temperature. Moreover, the full cells paired with $LiNi_{0.5}Co_{0.2}Mn_{0.3}O_2$, sulfur and thick $LiFePO_4$ cathodes (~2.8 mAh/cm^2) also show excellent cycling performances. The FGLA design provides a great opportunity for safe and high-energy SSLMBs.

View Article Online
DOI: 10.1039/D1EE03604A

Introduction

New battery technologies are highly demanded to tackle the deficiencies that have been identified in a conventional lithium-ion battery (LIB): energy density and safety.[1-3] To increase the energy density of a LIB, a Li metal anode (LMA), the "holy-grail" anode, has been recognized to be the ultimate choice due to its high specific capacity (3861 mAh/g) and low anode potential (–3.04 V vs. the standard hydrogen electrode).[4,5] However, the LMA suffers from severe Li dendrite growth, low Coulombic efficiency, and poor cycle life, as well as safety concerns in organic liquid electrolytes.[6,7] To circumvent these limitations, nonflammable solid-state electrolytes (SSE) are being intensively pursued.[8-12] Among all high Li-ion conductive SSEs, the garnet-structured oxide $Li_7La_3Zr_2O_{12}$ is more stable with LMA than other SSEs.[13-16] However, the garnet still faces two critical challenges: high contact resistance and severe Li dendrite growth.[17,18] The formation of Li dendrites depends on the potential distributions of Li near a Li/LLZTO interface (Fig. 1A). E_{Li}^0 and E_{SSE}^0 are defined as the thermodynamic equilibrium potentials of LMA and garnet, respectively, E_{Li} and E_{SSE} are the real potentials of LMA and garnet, respectively, under an overpotential η. If E_{SSE} is lower than 0 V, Li can nucleate and grow inside the SSE. The poor contact of garnet with LMA is due to the formation of lithiophobic Li_2CO_3 on a garnet surface, which significantly increases the interfacial resistance and polarization.[19-21] The electronic conductivity of 10^{-8} S·cm^{-1} in garnet may reduce the potential of garnet (E_{SSE}) to below zero at a high Li plating current, resulting in Li deposition inside the garnet (Fig. 1A and Fig. S1A).[22]

View Article Online
DOI: 10.1039/D1EE03604A

Extensive efforts have been devoted to reducing the interface resistance and the overpotential (η). Coating lithiophilic materials, such as Al_2O_3[23], Al[24], on garnet can wet the garnet with LMA because these coating materials can react with Li to form a lithiophilic Li-alloy interphase. However, these lithiophilic layers or alloys have high electronic conductivity and low interfacial energy against Li, which promotes both Li dendrite growth from the Li metal anode and direct Li deposition inside garnet (Fig. 1B).[22,25] Consequently, LLZO still has a low critical current density (CCD) of typically less than 1.0 mA/cm^2. In contrast, a lithiophobic and electronic insulating interlayer was used to suppress Li dendrites because the lithiophobic interlayer with weak bonding to Li promotes plane Li diffusion along the Li/interface and suppress the vertical growth through the interlayer for Li anodes.[26,27] Moreover, the low electronic conductivity of the interlayer also prevents the E_{SSE} from dropping to < 0 V even at a high current, thus suppressing Li deposition inside LLZO electrolytes. LiF has the highest interfacial energy and the lowest electronic conductivity (~10^{-31} S·cm^{-1}) among all interlayers, which can effectively suppress Li dendrite growth into SSE and Li deposition inside SSE even at a high Li plating overpotential. However, the super-lithiophobic LiF layer also leads to an ultra-poor contact and an ultra-high interfacial resistance at Li/LiF (Fig. 1C). The challenge is how to design an interphase layer that can simultaneously achieve a low interface resistance (lithiophilicity) and a high Li dendrite suppression capability (lithiophobicity), which is almost impossible with reported strategies.

View Article Online
DOI: 10.1039/D1EE03604A

In nature, biological functional gradient materials exist widely in the living organisms, such as bone, wood and nacre, where the structural and chemical gradients endow unprecedented functionalities compared to the conventional materials. More importantly, functional gradient materials can effectively fulfill multifunctional requirements within the limited space and components.[28,29] Inspired by the biological functional gradient structure, we developed a functional gradient Li metal anode (FGLA) that simultaneously solves the problems of poor contact and easy dendrite formation within a SSE (Fig. 1D). The unique FGLA can be obtained by a simple reaction between AlF_3 and excess molten Li, in which the formed LiAl spontaneously separates from LiF at high temperature resulting from the large interfacial energy differences between LiAl/Li and LiF/Li. In the LiF–Li_9Al_4 composition gradient layer, the LiF-rich component faces to the garnet SSE side and Li_9Al_4-rich component faces to the Li side. Lithiophobic LiF on the garnet surface can suppress Li dendrite penetration due to a high interface energy of LiF against Li, while the extremely low electronic conductivity of LiF also prevents the garnet potential ($E_{SSE}(x)$) from dropping to <0 V, inhibiting direct Li deposition within garnet (Fig. 1D). Moreover, lithiophilic Li_9Al_4 significantly reduces the interface resistance between Li garnet as well as the overpotential. The nature-inspired FGLA simultaneously reduced the interfacial resistance to ~1 Ω·cm^2 and increased the critical current density (CCD) to over 3.0 mA/cm^2 at room temperature (RT). Moreover, the cycling stability was extended to 600 h at RT. Full cells by pairing FGLA with $LiNi_{0.5}Co_{0.2}Mn_{0.3}O_2$, sulphur, or thick $LiFePO_4$ cathodes (~3.0 mAh·cm^{-2}), exhibited superior comprehensive

View Article Online
DOI: 10.1039/D1EE03604A

performances. The concept of forming gradient layer distinguishes from previously reported AlF_3-modified separator and Li-AlF_3 composite in liquid batteries, where only lithiophobic–lithiophilic mixture was formed on Li anodes.[30,31]

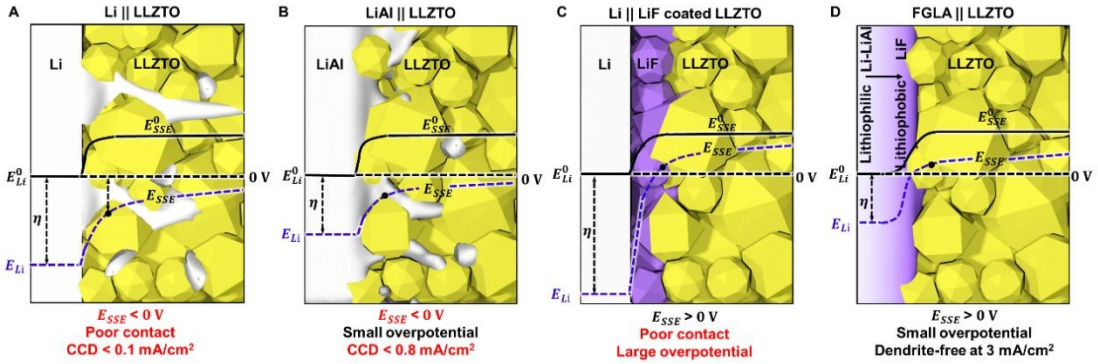

Fig. 1 Diagram of the potential distribution of Li near a Li/LLZTO interface during the plating process. (A) Li metal exhibits a poor interfacial contact with a LLZTO pellet. Dendritic Li and a short-circuit occur at a very low CCD (0.1 mA·cm^{-2}) due to the large interfacial resistance and electron conducting interface. (B) Lithiophilic LiAl alloy can achieve an intimate contact with LLZTO. (C) Coating LLZTO with a layer of electronic insulating, lithiophobic LiF with a high interfacial energy can increase E_{SSE} within LLZTO and prevent Li dendrites from depositing inside LLZTO. (D) Engineering a gradient FGLA anode effectively increases E_{SSE} of LLZTO without sacrificing the interface contact. The gradient anode can suppress Li dendrite formation under a current density over 3.0 mA·cm^{-2} at RT and 25 mA/cm^2 at 60 °C.

RESULTS AND DISCUSSION

Phase separation in multiple compositions has been widely used to design functional gradient materials. Phases with quite different surface and interface energies tend to separate from each other. FGLA was formed by adding AlF_3 powder (Fig. 2A,

View Article Online
DOI: 10.1039/D1EE03604A

Fig. S2 and S3) into molten Li, where AlF_3 experienced conversion and alloying reactions to generate a LiAl and LiF composite (more details on the synthetic procedure in experimental procedures). The final composite at different mass ratio of Li to AlF_3 can be obtained from the ternary phase diagram of the Li-Al-F_2 system (Fig. 2B) and thermodynamic calculations (Table S1). To balance the interface wettability and the specific capacity of FGLA, the Li/AlF_3 mass ratio was optimized as 2:1 (Fig. S4 and S5). X-ray diffraction (XRD) patterns in Fig. 2C confirm that the Li-AlF_3 (2:1) composite consists of LiF, Li_9Al_4, and excess Li.

The phase separation of FGLA was analyzed with thermodynamical derivation and DFT calculations. In a Li-X binary phase system (X represents the other phase), the distribution of X on the surface (n_X) or in the bulk (N_X) of the Li composite depends on the total energy and can be quantified (see Supplementary Note 1 for more details),

$$\frac{n_X}{n_{Li}} = \frac{N_X}{N_{Li}} \times e^{-\frac{0.5\,(\gamma_X - \gamma_{X-Li}) \times s_X}{kT}} \quad (1)$$

where *n* and *N* are numbers of particles on the surface and in the bulk, respectively. γ_X is the surface energy of *X*, while $\gamma_{X\text{-}Li}$ is the interfacial energy between *X* and Li. S_X is the surface area of a single *X* particle. *k* and *T* are the Boltzmann constant and the absolute temperature. According to the thermodynamic analysis, the difference between the surface energy (γ_X) of *X* and the interfacial energy ($\gamma_{X\text{-}Li}$) of *X/Li* can serve as the driving force for phase separation in the Li-X system. In the case of $\gamma_X < \gamma_{X\text{-}Li}$, $\frac{n_{LiF}}{n_{Li}}$ is larger than $\frac{N_{LiF}}{N_{Li}}$, indicative of a higher concentration of *X* on the surface. On the contrary, *X* presents a higher concentration in the bulk where $\gamma_X > \gamma_{X\text{-}Li}$. For Li-$AlF_3$ with a mass ratio of 2:1, Li-Al is liquid at 300 °C (see Li-Al phase diagram[33] in Fig. S7 and

View Article Online
DOI: 10.1039/D1EE03604A

its corresponding description) while the formed LiF is in solid state, since the melting point of LiF is as high as 848.2 °C. LiF is strongly lithiophobic at a high temperature of ~300 °C as evidenced by a high contact angle of about 120º (Fig. S16C and S16E). According to the Young equation ($\gamma_{LiF} - \gamma_{LiF-Li} = \gamma_{Li}\cos\theta$), $\gamma_{LiF} - \gamma_{LiF-Li}$ is about -0.21 J/m^2 at ~300 °C.[32] Assuming that the radius of LiF particle is about 5 nm, $\frac{n_{LiF}}{n_{Li}}$ is more than e^{1000} times larger than $\frac{N_{LiF}}{N_{Li}}$, suggesting that LiF are enriched on the surface of the liquid Li-Al composite. The process of LiF migration from the liquid LiAl alloy to surface was shown in Fig. S8. After solidification, the surface energy (LiF and Li_9Al_4) and interfacial energy (LiF/Li and Li_9Al_4/Li) were further calculated by DFT methods (See more details in Supplementary Note 1). Fig. 2D presents the atomic structures of LiF and Li_9Al_4, as well as the interface models of LiF/Li and Li_9Al_4/Li. As shown in Fig. 2E, LiF exhibits an extreme lithiophobicity ($\gamma_{LiF} - \gamma_{LiF-Li} = -0.47$ J/m^2) at solid-state,[26] thus it would maintain a high concentration on the surface. By contrast, Li_9Al_4 has a low interface energy $\gamma_{Li9Al4\text{-}Li}$ of 0.004 J/m^2, but a high surface energy γ_{Li9Al4} of 0.83 J/m^2. Therefore, Li_9Al_4 is highly lithiophilic and tends to exist within the bulk composite. Apparently, such a large energy difference drives the Li-Li_9Al_4-LiF composite to thermodynamically form a FGLA, as shown in Fig. 2F.

The composition gradient of the FGLA was validated using depth-profiling time-of-flight secondary-ion mass spectroscopy (ToF-SIMS) in a negative mode (Fig. S9). As shown in Fig. S10, the F^- signal, which represents LiF, maintained a high level on the surface layer and began to gradually decrease after 2000 s sputtering. In sharp contrast, the Al^- signal is too weak to be detected on the surface of the FGLA and

View Article Online
DOI: 10.1039/D1EE03604A

gradually increases after 2000 s sputtering. The phase gradient of LiF and Li_9Al_4 in FGLA was clearly demonstrated. Accordingly, Fig. 2G-2I show the corresponding 3D images of FGLAs with sputtering time, which obviously shows a gradient composition that is in line with the results predicted by DFT calculations. X-ray photoelectron spectroscopy (XPS) combined with Ar^+ ion sputtering also confirmed the successful formation of a FGLA by reacting AlF_3 with molten Li (see Fig. S11 and its descriptions).

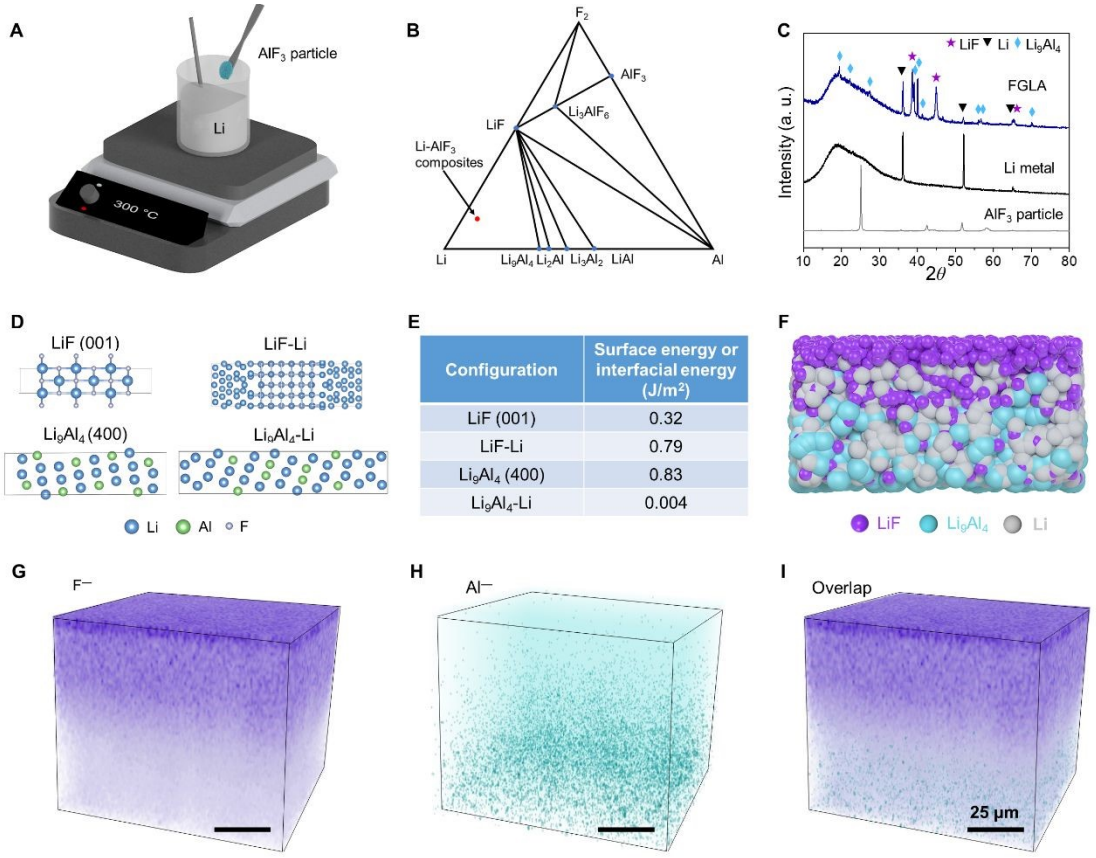

Fig. 2 The synthesis, DFT calculations as well as characterizations of the gradient FGLA. (A) Schematic illustration of the synthetic process for the composite. (B) Ternary phase diagram of Li-Al-F_2 system. (C) XRD patterns of AlF_3 particle, Li, and FGLA. (D) Atomic structures for the LiF (001), LiF/Li interface, Li_9Al_4 (400) and Li_9Al_4/Li interface. (E) The surface energies of LiF (001) and Li_9Al_4 (400), and interfacial energies of LiF/Li interface and Li_9Al_4/Li interface. (F) A schematic

View Article Online
DOI: 10.1039/D1EE03604A

representation of the FGLA. Since Li_9Al_4 is strongly lithiophilic and LiF is highly lithiophobic, Li_9Al_4 on Li side (bottom) and LiF on the other side (top) forms Li-Li_9Al_4-LiF composition gradient composite materials. (G) F^-, (H) Al^- and (I) the overlap in the ToF-SIMS sputtered volumes of the FGLA, showing a gradience.

A garnet-type $Li_{6.5}La_3Zr_{1.5}Ta_{0.5}O_{12}$ (LLZTO) SSE was adopted in this study due to its high conductivity and stability against Li metal for the following tests. The details on the synthetic procedure and characterizations of LLZTO pellets can be found in experimental procedures and Fig. S12. The wettability of Li on LLZTO was evaluated by measuring the contact angle (CA) of liquid Li metal droplets. Pristine Li exhibits a spherical shape on LLZTO surface with a CA of ~105º due to the existence of a Li_2CO_3 surface (Fig. S16A). Using Li-Al alloy (Fig. S13), the CA was reduced to ~70º (Fig. S16B), showing a better interface contact. After coating a thin layer of LiF on LLZTO (see more details in Methods and Fig. S14 and Fig. S15), the CA of Li or LiAl on LLZTO increased to 120º (Fig. S16C). However, the FGLA droplet can easily spread on LLZTO with a small CA of 70º (Fig. S16D), which demonstrates that lithiophilic Li_9Al_4 in the composite greatly improves the interface wetting and the *in-situ* formed LiF on LLZTO does not affect the interface contacts. Next, the interface contacts between LLZTO and different Li anodes were characterized with SEM. Obviously, gaps appeared at the interface of Li/LLZTO and Li/LiF-coated LLZTO while intimate contact was observed in LiAl/LLZTO or FGLA/LLZTO interfaces (Fig. S17). This observation highlights the importance of wettability in interface contact.

View Article Online
DOI: 10.1039/D1EE03604A

The composition gradient at a FGLA/LLZTO interface was also thermodynamically analyzed with DFT calculations. The atomic structures of LiF-LLZO (Li_9Al_4-LLZO) and corresponding interfacial energies are displayed in Fig. 3A and Fig. S6. LiF shows a lower $\gamma_{LiF\text{-}LLZO}$ (0.65 J/m^2) than $\gamma_{LiF\text{-}Li}$ (0.79 J/m^2), indicating an enrichment of LiF at the Li-LLZTO interface, while Li_9Al_4 presents a much higher $\gamma_{Li9Al4\text{-}LLZO}$ (0.75 J/m^2) than $\gamma_{Li9Al4\text{-}Li}$ (0.004 J/m^2), tending to concentrate in the bulk of Li (see Supplementary Note 1 for more details). These results suggest that a FGLA can be constructed at a Li/LLZTO interface, as displayed in Fig. 3B. We further employed energy dispersive X-ray spectroscopy (EDX) and ToF-SIMS measurements to characterize the gradient structure of the FGLA/LLZTO interface. The composition changes along a line from FGLA to LLZTO near the interface (Fig. 3C and 3D) was monitored with EDX. Inside the FGLA anode (~0.2 μm from the scanning), LiF presents a low concentration while LiAl alloy delivers a higher concentration, depicting the higher concentration of lithiophilic LiAl than lithiophobic LiF in the bulk FGLA. Upon reaching to the FGLA/LLZTO interface, the concentration of LiF increases rapidly while LiAl quickly decreases. In the region of 0.5 to 1.3 μm, LiF maintains a much higher content than LiAl, and then LiF starts to drop to a low value after crossing the FGLA/LLZTO interface at 1.3 μm, while LLZTO starts to increase quickly after 1.5 μm, proving the existence of a LiF-rich layer on the LLZTO surface. Furthermore, depth-profiling ToF-SIMS images were collected on the FGLA/LLZTO interface as well (Fig. 3E-3H). Obviously, the F^- signal, representing LiF, exhibits a much higher intensity within ~2 μm of the interface than in the bulk FLGA, strongly demonstrating the enrichment of LiF near the interface. Overall, the FGLA not only presents great wettability with LLZTO, but also forms a gradient structure on the LLZTO surface to suppress Li dendrites.

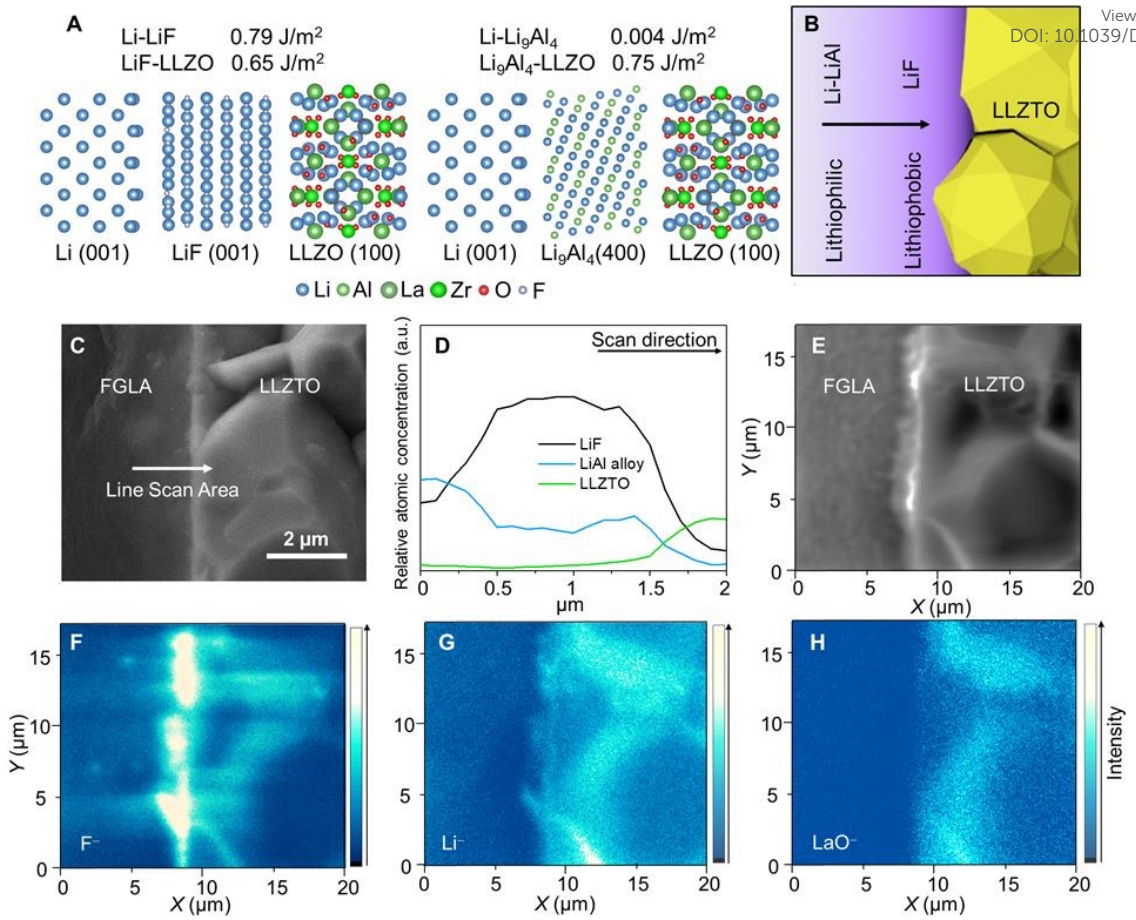

Fig. 3 The composition distribution of FGLA at the FGLA/LLZTO interface. (A) The atomic structures of the Li, LiF, LLZO and Li_9Al_4, as well as their interfacial energies. (B) A schematic diagram of the FGLA on LLZTO surface. (C) SEM and (D) corresponding EDX line scanning images of the FGLA/LLZTO interface. (E-H) Depth-profiling ToF-SIMS images of the FGLA/LLZTO interface. F^- and LaO^- signals represent LiF and LLZTO, respectively.

The Li plating/stripping performance of three Li anodes (Li, LiAl, and FGLA) were evaluated at 25 ºC in solid-state symmetric cells with LLZTO as the SSE. The interface resistances of these cells were evaluated with electrochemical impedance spectroscopy (EIS). A large interface area-specific resistance (semi-circle) >1070

View Article Online
DOI: 10.1039/D1EE03604A

$\Omega \cdot cm^2$ was given in a Li|garnet|Li symmetric cell due to the poor contact of pristine Li on LLZTO (EIS, Fig. 4A). Coating LiF on LLZO further increased the interface resistance to ~1.8×10^5 $\Omega \cdot cm^2$, Fig. 4C. Notably, the LiAl|garnet|LiAl cell with LiAl alloy electrodes exhibits a much smaller interfacial resistance (<7 $\Omega \cdot cm^2$), which is beneficial from a significantly improved interface wetting (Fig. 4B). As expected, a FGLA|LLZTO|FGLA cell further reduced the interfacial resistance to ~1 $\Omega \cdot cm^2$, demonstrating the superior properties of the *in-situ* formed Li-LiAl-LiF gradient.

For a solid-state Li metal battery, an essential parameter for solid state electrolyte is the critical current density (CCD), which is defined as the current density above which Li dendrite grows through a SSE and leads to a short-circuit. CCD represents the capability of the electrolyte for Li dendrite suppression. The CCDs of these symmetric cells at room temperature were measured in galvanostatic Li plating/stripping cycles at stepwise current densities; each plating/stripping time was fixed at 0.5 hour. As shown in Fig. 4D, short-circuit occurs quickly in the Li|LLZTO|Li cell at a low CCD of about 0.1 $mA \cdot cm^{-2}$. Due to the enhanced interface wetting and smaller interfacial resistance, the LiAl|LLZTO|LiAl cell showed a CCD of 0.8 $mA \cdot cm^{-2}$ (Fig. 4E). When LiF is coated on the LLZTO surface, the Li|LiF-coated LLZTO|Li cell shows a large Li plating/stripping overpotential of 5.0 V at a low current of 0.05 $mA \cdot cm^{-2}$ (Fig. S18) due to a large interface resistance at the Li|LiF surface. As expected, the FGLA|LLZTO|FGLA cell shows stable plating/stripping performances even at a high current density of 3.0 $mA \cdot cm^{-2}$ and a high capacity of 1.5 $mAh \cdot cm^{-2}$ (Fig. 4F) due to the perfect interface contact and the *in-situ* formed LiF layer on the LLZTO surface.

View Article Online
DOI: 10.1039/D1EE03604A

More importantly, at a high current density of 3.0 mA/cm^2, voltage polarization has reached to 5.0 V, but short-circuit is still not observed (EIS profiles of the cell before and after CCD measurement are shown in Fig. S19), indicative of a dendrite-free plating/stripping behavior. The increase of polarization may be caused by voids accumulations near the interfaces.[34,35] To reduce the influences of voids, the charging/discharging capacity was fixed to measure CCDs of FGLA|LLZTO|FGLA cells. Surprisingly, CCDs of 9.0 mA/cm^2 at RT (Fig. S20A) and 25.0 mA/cm^2 at 60 °C (Fig. S20B) were achieved (CCD comparison between this work and previous works is shown in Table S3). The FGLA|LLZTO|FGLA cell also exhibits low and stable overpotentials upon long-term cycling for 670 h (Fig. 4G). Moreover, the symmetric cell with FGLA electrodes delivers stable and smooth cycling plateaus at large current densities of 2.0 and 5.0 mA·cm^{-2} at RT (Fig. 4H). The overall investigations on interfacial resistance, CCD, and cycling durations clearly indicate that the FGLA can provide a superior interface compatibility and dendrite suppression ability with an LLZTO electrolyte, enabling fast charging/discharging of solid-state garnet Li batteries.

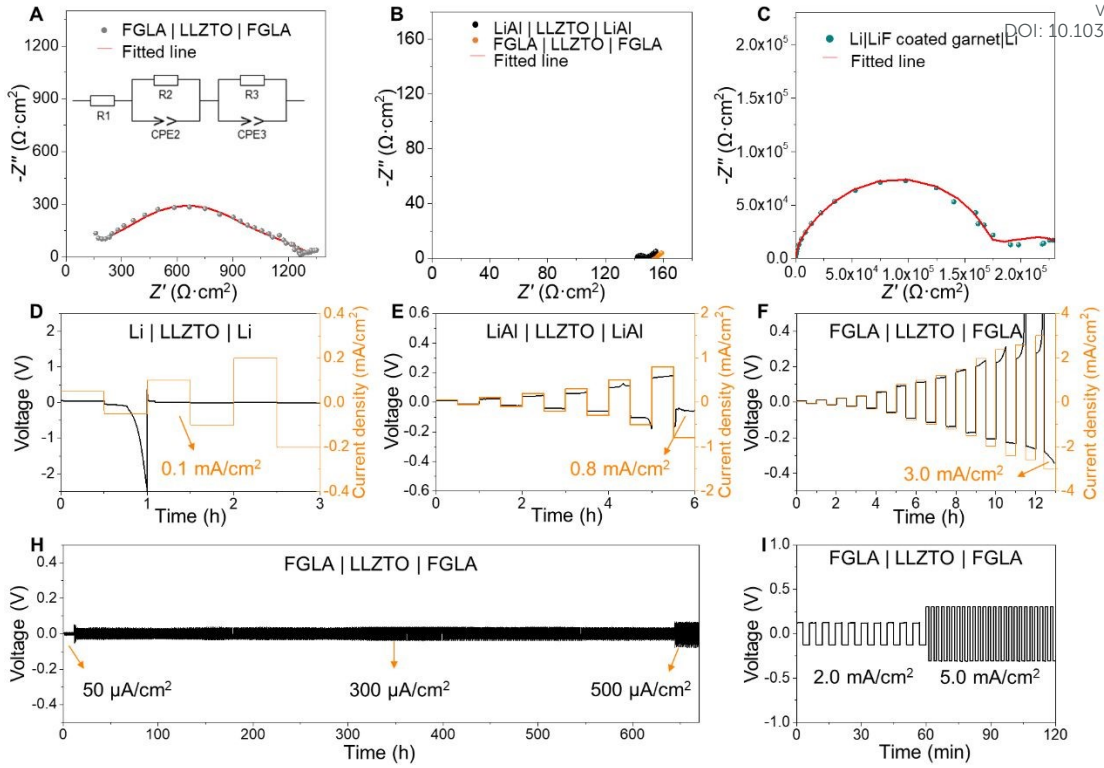

Fig. 4 Electrochemical characterization of FGLA in a solid-state symmetric cell and comparisons to reference Li metal-based anodes. (A) Electrochemical impedance spectra (EIS) of symmetric cells with FGLA or other Li-based electrodes at room temperature. (B) Image expansion corresponding to the area outlined by the orange square in (A). (C) EIS of Li|LiF-coated LLZTO|Li symmetric cell at room temperature. The resistance comparison agrees well with the result of interface wettability. CCD measurements of (D) Li|LLZTO|Li, (E) LiAl|LLZTO|LiAl, and (F) FGLA|LLZTO|FGLA symmetric cells. (G) Cycling performance of FGLA|LLZTO|FGLA symmetric cell, showing a long-term stability at room temperature. (H) Galvanostatic cycling of the FGLA|LLZTO|FGLA symmetric cell at 2.0 and 5.0 mA·cm^{-2}, at room temperature.

Given the highly stable FGLA|LLZTO interface, FGLA was further evaluated in

View Article Online
DOI: 10.1039/D1EE03604A

full cells by pairing with $LiNi_5Co_2Mn_3O_2$ (NCM523), sulfur (S) or thick $LiFePO_4$ (LFP) cathodes. To reduce the interfacial resistance between LLZTO pellet and cathode, a tiny amount of liquid electrolyte was added at the cathode side, which was a commonly used strategy in garnet-based full cells.[23,24] Details of the cell assembly are available in Methods. The EIS result of the FGLA|LLZTO|NCM523 cell was shown in Fig. 5A. The total impedance of the FGLA|LLZTO|NCM523 cell contains the resistance of LLZTO pellet and interfacial resistances between LLZTO pellet and electrodes. The LLZTO pellet shows an impedance of about 72 $\Omega \cdot cm^2$. Benefiting from the ignorable interfacial resistance between LLZTO and FGLA and the improved interface contact at cathode side with a liquid electrolyte, the overall resistance is as small as 155 $\Omega \cdot cm^2$. As shown in Fig. 5B, the FGLA|LLZTO|NCM523 cell delivers a specific capacity of 165 $mAh \cdot g^{-1}$ (0.46 $mAh \cdot cm^{-2}$) at 1 C. Moreover, an average Coulombic efficiency of ~99.3% as well as a high capacity retention of 85.5% for 300 cycles is given (Fig. 5C). Furthermore, full cells with a higher NCM523 mass loading were tested at a higher current density. The solid-state cell exhibits a capacity of 139 $mAh \cdot g^{-1}$ (0.53 $mAh \cdot cm^{-2}$) at 2 C and retains 80% of the specific capacity after 200 cycles (Fig. S21).

To demonstrate the versatility of the FGLA, FGLA|LLZTO|S full cells were assembled with a sulfur/carbon (S/C) cathode. Such a chemistry promises an attractive theoretical energy density.[36] Although Li-S batteries have been well-investigated, their cyclability has always been hindered by the dissolution and shuttle effect of a S cathode as well as by an unstable Li metal anode in liquid electrolyte system.[37,38] As expected, the capacity of a conventional liquid Li-S cell started to decay from the beginning (Fig.

View Article Online
DOI: 10.1039/D1EE03604A

5D). After 300 cycles at 0.2 C, the liquid Li-S cell only delivers a capacity of 181 $mAh \cdot g^{-1}$ and exhibits an average Coulombic efficiency of only 79.6%, which corresponds to a capacity retention of 18% (Fig. S22). On the other hand, the FGLA|LLZTO|S cell offered a capacity of 870.0 $mAh \cdot g^{-1}$ (0.96 $mAh \cdot cm^{-2}$) after 300 cycles with an average Coulombic efficiency of 99.9%, corresponding to a much higher capacity retention of 71%. More critically, the FGLA|LLZTO|S cell can still deliver a capacity of 620 mAh/g with an average capacity decay of 0.024% per cycle over 2000 cycles (Fig. S23), far exceeding the liquid Li-S cell (0.080%, 300 cycles, Fig. 5D). As shown in Fig. S23B, we can find that the interfacial resistance of the FGLA|LLZTO|S cell is nearly the same before and after 2000 cycles. All the improvements can be credited to the effectiveness of a dense LLZTO for eliminating the shuttle effect and the superiority of the highly stable FGLA|LLZTO interface. Next, a thick LFP cathode with a mass loading of about 18 mg/cm^2 was paired with FGLA|LLZTO to further evaluate the performance of the FGLA. As shown in Fig. S24A, the FGLA|LLZTO|LFP cell exhibits an areal capacity of about 2.85 $mAh \cdot cm^{-2}$. More importantly, the cell achieved a stable cycling performance of 80 cycles with a capacity retention of 93% (Fig. S24B), exhibiting the great capability of FGLA/LLZTO interface to stabilize a large areal capacity. Apparently, the FGLA with its unique gradient structure on LLZTO SSE, enables full cells with an excellent cycling performance and an areal capacity that has not been observed in any LLZTO based full cells known thus far (Table S4).

View Article Online
DOI: 10.1039/D1EE03604A

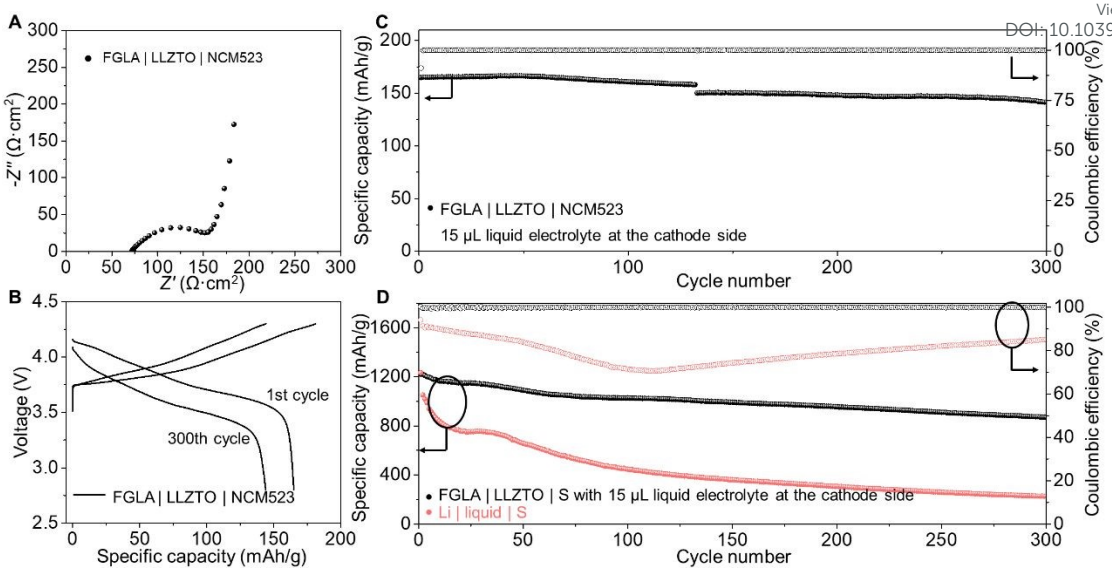

Fig. 5 Electrochemical characterizations of the FGLA in full cells at RT. (A) Nyquist plot of a FLGA|LLZTO|NCM523 cell at RT. (B) The charge-discharge curves of the 1st cycle and the 300th cycle of the FGLA|LLZTO|NCM523 cell at 1 C. (C) Cycling stability of the FGLA|LLZTO|NCM523 cell at 1 C (170 $mA \cdot g^{-1}$). (D) Cycling stability comparison of the FGLA|LLZTO|S cell versus the liquid Li-S cell at 0.2 C (1 C = 1675 $mA \cdot g^{-1}$). 15 μL liquid electrolyte was added at the cathode side.

Conclusion

Driven by the large interfacial energy differences between Li/LiAl and Li/LiF, we have developed a self-regulated FGLA that displays all the benefits of interface enhancement. Intimate contact of the Li with an *in-situ* formed lithiophilic Li_9Al_4 layer reduces the interfacial resistance, while the *in-situ* formed lithiophobic LiF layer effectively suppresses Li dendrites due to a high interfacial energy to Li and low electronic conductivity, which was proven by a high critical current density over 3.0 $mA \cdot cm^{-2}$ at room temperature. The as-prepared solid-state symmetric cell with the

View Article Online
DOI: 10.1039/D1EE03604A

gradient FGLA can deliver stable plating/stripping for up to 670 h with limited polarization at RT. Leveraging the unprecedented performance of a FGLA|LLZTO interface, the corresponding assembled full cells all showed excellent performances. For example, the FGLA|LLZTO|NCM523 full cell delivers a cyclability with an 85.5% capacity retention after 300 cycles at 1 C. Even in the more challenging Li-S system, the FGLA|LLZTO|S cell also offers a high capacity of 620 $mAh \cdot g^{-1}$ after 2000 cycles. In particular, the exciting capability of FGLA with thick LFP electrodes (with a loading of 2.85 $mAh \cdot cm^{-2}$) shows a great potential to be practically applied. In general, the universal concept of self-regulated FGLA can effectively reduce interface resistance and suppress Li dendrites at the same time, which is also applicable to other solid-state battery systems and even to liquid Li batteries for practical application.

View Article Online
DOI: 10.1039/D1EE03604A

EXPERIMENTAL PROCEDURES

Synthesis of FGLA and LiAl alloy

To prepare FGLA, Li foil was placed in a stainless-steel container and heated at 300 °C on a hot plate. The native surface film was removed carefully to give a shiny liquid Li. A certain amount of AlF_3 powder was added slowly to the container and vigorously stirred for about 0.5 h. Then, the container was cooled down to room temperature by moving from the hot plate. The resulting solid was collected. The preparation of LiAl alloy is similar to the procedure for preparing FGLA by replacing AlF_3 with Al foil. Note that all the synthesis processes were carried out in an Argon-filled glovebox with the concentrations of moisture and oxygen < 0.1 ppm.

Material characterizations

The ternary phase diagram and corresponding computation data were from the Materials Project (MP).[39] XRD patterns were conducted by DX2700 (shjingmi corporation) at a scanning speed of 10 °·min^{-1}. The morphology was investigated by scanning electron microscopy (SEM, sigma 300 vp, ZEISS). Surface chemical composition analysis was characterized with XPS (American Thermo Fisher Scientific ESCALAB 250Xi). The depth-profiling XPS analysis was conducted with Ar^+ ion sputtering. The sputtered thickness was determined by the sputtering time multiplied by sputtering speed (2.7 Å·s^{-1}). ToF-SIMS analysis was taken using an instrument (IONTOF GmbH) from Münster, Germany, with a pulsed Ga^{3+} primary ion beam in a negative mode.

View Article Online
DOI: 10.1039/D1EE03604A

Computational methods.

The DFT calculations[40,41] are performed by using Vienna Ab-initio Simulation Package (VASP)[42] with Projector Augmented Wave (PAW) method.[43] And the exchange-correlation energy is described by the functional of Perderw, Burke, and Ernzerhof (PBE) form[44,45] including van der Waals corrections (DFT-D3 method).[46] The kinetic energy cutoff of electron wave functions is 520 eV. The geometry optimizations are performed by using the conjugated gradient method, and the convergence threshold is set to be 10^{-4} eV in energy and 0.02 eV $Å^{-1}$ in force. The Brillouin zone is sampled by using the Monkhorst−Pack scheme.[47] The interface energy was evaluated using the same method in a previous work.[26] Visualization of the electrolyte structures are made by using VESTA.[48]

Contact angle measurements

LLZTO pellets were prepared according to previous reports and carefully polished with sand papers to give a smooth surface. LiF-coated LLZTO was obtained by coating a polished LLZTO pellet with LiF. The detailed preparation and coating parameters can be found in the supporting information. Various Li metal-based materials, polished LLZTO pellets, and LiF-coated LLZTO pellets were placed on a hot plate at 300 °C. Liquid droplets of pure Li, Li-Al alloy or Li-AlF_3 composite were then deposited onto the testing pellets to measure the CA. Note that all the measurements were carried out in an Argon-filled glovebox with the concentrations of moisture and oxygen < 0.1 ppm.

Electrochemical performance measurements

2032-type coin cells were used in this study. The stacking pressures were ~3.4 MPa

View Article Online
DOI: 10.1039/D1EE03604A

during cell assembly. We did not apply extra stress during cell testing and the pressure conditions for all cells were the same. To sandwich LLZTO with two FGLA electrodes, we prepared one side by one side. Typically, FGLA in a stainless-steel container was placed on a hot plate (300 °C) in an Ar-filled glovebox. Then, a LLZTO pellet was placed on the FGLA and rubbed in the container. After about 1 minute, one side of the LLZTO pellet was fully covered by FGLA. Then, another side was treated using the same method. After both sides were covered with FGLA, the sandwich structure was kept at 300 °C to form a self-regulated gradient interphase, followed by cooling down to room temperature and coin-cell assembling.

The Li|LiF-coated garnet|Li symmetric cell was sandwiched by two identical pure Li electrode at 300 °C. An AC amplitude of 10 mV and frequencies from 1 MHz to 10 mHz were utilized to measure the EIS profiles. EISs were tested with a Biologic workstation (VMP3) at RT.

CCD measurements were conducted with gradually increasing current densities and each charge/discharge step was fixed to 30 min. As for CCD tests at 60 °C, the capacity was fixed with stepwise current densities.

To fabricate full cells, different cathodes were prepared, and 2032-type coin cells were used. NCM523 electrodes were prepared by mixing NCM523, carbon black and polyvinylidene fluoride (PVDF) binder with a mass ratio of 90:5:5 in N-methyl-2-pyrrolidinone (NMP) to form a slurry, which was then cast onto Al foil and dried at 90 °C under vacuum overnight. The S/C cathode was prepared via a simple freeze-drying method. 80 wt% sulfur/Kejten black was mixed with 10 wt% super P and 10 wt%

View Article Online
DOI: 10.1039/D1EE03604A

LA133 binder. After being cast onto carbon-coated Al foil, the electrode was frozen to dry at -20 °C under vacuum. The mass loading of sulfur was ~1.1 mg·cm^{-2}. A thick LFP cathode was commercially available and the loading was about 2.8 mAh·cm^{-2}. The fabrication process of anode side was the same as that in the symmetric cells and 15 μL electrolyte was dropped on the cathode side to wet the cathode/garnet interface.

To assemble Li|liquid|NCM523 full cells, celgard-2400 membranes and 60 μL electrolyte (1.0 M $LiPF_6$ in EC/DEC(v/v=1:1) with 10% FEC and 1% VC as additives) were used. In Li-S cells, the electrolyte was 1.0 M lithium bis(trifluoromethanesulfonyl)imide (LiTFSI) dissolved in tetraethylene glycol dimethyl ether (TEGDME) solvent with 0.1 M Li_2S and 0.1 M P_2S_5 as additives. To assemble liquid Li-S full cells, 60 μL electrolyte was added with celgard-2400 separators. In Li|liquid|LFP full cells, 60 μL electrolyte (1.0 M $LiPF_6$ in EC/DEC(v/v=1:1) with 10% FEC and 1% VC as additives) was added with celgard-2400 separators. Symmetric cells and full cells were tested with Neware CT-4008T-5V20mA-164 battery tester.

Author contributions

W. L., T. R. W., C. S. W., Y. H. H. and J. B. G. conceived of the idea for the project. T. R. W. and J. D. prepared the samples and constructed the tests. B. Z., J. X., and C. S. W. conducted the theoretical computations. T. R. W., J. D., H. H. X., Y. H., L. Q. H., Z. Y. S and J. Y. W. prepared the electrodes and conducted the battery tests. W. L., T. R. W., B. Z., C. S. W., Y. H. H. and J. B. G. prepared the manuscript.

View Article Online
DOI: 10.1039/D1EE03604A

Conflicts of interest

The authors declare no competing financial interests.

Acknowledgements

Funding

We acknowledge the financial support by National Natural Science Foundation of China (92163120) and "Shanghai Rising-Star Program" (19QA1409300). We acknowledge Prof. Xiangxin Guo and Prof. Ning Zhao from Qingdao University for their assistance on preparing garnet pellets. We acknowledge Prof. Huanan Duan, Mr. Hongpeng Zheng from Shanghai Jiaotong University for their assistance on ToF-SIMS measurements.

References

1. X. L. Ji, *Energy Environ. Sci.*, **2019**, 12, 3203.
2. X. W. Shen, Y. T. Li, T. Qian, J. Liu, J. Q. Zhou, C. L. Yan and J. B. Goodenough, *Nat. Commun.*, 2019, **10**, 900.
3. A. M. Hafez, Y. C. Jiao, J. J. Shi, Y. Ma, D. X. Cao, Y. Y. Liu and H. L. Zhu, *Adv. Mater.*, 2018, **30**, 1802156.
4. W. Xu, J. Wang, F. Ding, X. Chen, E. Nasybulin, Y. Zhang and J.-G. Zhang, *Energy Environ. Sci.*, 2014, **7**, 513-537.
5. Y. Lu, Z. Tu and L. A. Archer, *Nat. Mater.*, 2014, **13**, 961-969.
6. J. Li, S. Basu, Y. P. Wang, Z. Z. Chen, P. Hundekar, B. W. Wang, J. Shi, Y. F. Shi, S. Narayanan and N. Koratkar, *Science*, 2018, **359**, 1513-1516.

View Article Online
DOI: 10.1039/D1EE03604A

7. X. B. Cheng, R. Zhang, C. Z. Zhao and Q. Zhang, *Chem. Rev.*, 2017, **117**, 10403-10473.

8. Z. Y. Tu, S. Choudhury, M. J. Zachman, S. Y. Wei, K. H. Zhang, L. F. Kourkoutis and L. A. Archer, *Nat. Energy*, 2018, **3**, 310-316.

9. J. Janek and W. G. Zeier, *Nat. Energy*, 2016, **1**, 16141.

10. A. Manthiram, X. Yu and S. Wang, *Nat. Rev. Mater.*, 2017, **2**, 16103.

11. H. Y. Huo, J. Gao, N. Zhao, D. X. Zhang, N. G. Holmes, X. N. Li, Y. P. Sun, J. M. Fu, R. Y. Li, X. X. Guo and X. L. Sun, *Nat. Commun.*, 2021, **12**, 176.

12. F. P. Zhao, Q. Sun, C. Yu, S. M. Zhang, K. Adair, S. Z. Wang, Y. L. Liu, Y. Zhao, J. W. Liang, C. H. Wang, X. N. Li, X. Li, W. Xia, R. Y. Li, H. Huang, L. Zhang, S. Q. Zhao, S. G. Lu and X. L. Sun, *ACS Energy Lett.*, 2020, **5**, 1035-1043.

13. R. Murugan, V. Thangadurai and W. Weppner, *Angew. Chem. Int. Ed.*, 2007, **46**, 7778-7781.

14. S. Afyon, F. Krumeich and J. L. M. Rupp, *J. Mater. Chem. A*, 2015, **3**, 18636-18648.

15. T. Krauskopf, R. Dippel, H. Hartmann, K. Peppler, B. Mogwitz, F. H. Richter, W. G. Zeier and J. Janek, *Joule*, 2019, **3**, 2030-2049.

16. J. van den Broek, S. Afyon and J. L. M. Rupp, *Adv. Energy Mater.*, 2016, **6**, 1600736.

17. R. H. Basappa, T. Ito and H. Yamada, *J. Electrochem. Soc.*, 2017, **164**, A666-A671.

18. E. J. Cheng, A. Sharafi and J. Sakamoto, *Electrochim. Acta*, 2017, **223**, 85-91.

19. L. Cheng, E. J. Crumlin, W. Chen, R. M. Qiao, H. M. Hou, S. F. Lux, V. Zorba, R. Russo, R. Kostecki, Z. Liu, K. Persson, W. L. Yang, J. Cabana, T. Richardson, G. Y. Chen and M. Doeff, *Phys. Chem. Chem. Phys.*, 2014, **16**, 18294-18300.

View Article Online
DOI: 10.1039/D1EE03604A

20. A. Sharafi, E. Kazyak, A. L. Davis, S. Yu, T. Thompson, D. J. Siegel, N. P. Dasgupta and J. Sakamoto, *Chem. Mater.*, 2017, **29**, 7961-7968.

21. J. F. Wu, B. W. Pu, D. Wang, S. Q. Shi, N. Zhao, X. X. Guo and X. Guo, *ACS Appl. Mater. Inter.*, 2019, **11**, 898-905.

22. F. D. Han, A. S. Westover, J. Yue, X. L. Fan, F. Wang, M. F. Chi, D. N. Leonard, N. J. Dudney, H. Wang and C. S. Wang, *Nat. Energy*, 2019, **4**, 187-196.

23. X. G. Han, Y. H. Gong, K. Fu, X. F. He, G. T. Hitz, J. Q. Dai, A. Pearse, B. Y. Liu, H. Wang, G. Rubloff, Y. F. Mo, V. Thangadurai, E. D. Wachsman and L. B. Hu, *Nat. Mater.*, 2017, **16**, 572-579.

24. K. K. Fu, Y. H. Gong, B. Y. Liu, Y. Z. Zhu, S. M. Xu, Y. G. Yao, W. Luo, C. W. Wang, S. D. Lacey, J. Q. Dai, Y. N. Chen, Y. F. Mo, E. D. Wachsman and L. B. Hu, *Sci. Adv.*, 2017, **3**, e1601659.

25. Y. L. Song, L. Y. Yang, W. G. Zhao, Z. J. Wang, Y. Zhao, Z. Q. Wang, Q. H. Zhao, H. Liu and F. Pan, *Adv. Energy Mater.*, 2019, **9**, 1900671.

26. X. L. Fan, X. J, F. D. Han, J. Yue, J. Chen, L. Chen, T. Deng, J. J. Jiang, C. S. Wang, *Sci. Adv.*, 2018, **4**, eaau9245.

27. X. Ji, S. Hou, P. F. Wang, X. Z. He, N. Piao, J. Chen, X. L. Fan and C. S. Wang, *Adv. Mater.*, 2020, 32(46), 2002741.

28. X. Y. Li, L. Lu, J. G. Li, X. Zhang and H. J. Gao, *Nat. Rev. Mater.*, 2020, **5**, 706-723.

29. Z. Q. Liu, M. A. Meyers, Z. F. Zhang and R. O. Ritchie, *Prog. Mater. Sci.*, 2017, **88**, 467-498.

30. H. S. Wang, D. C. Lin, Y. Y. Liu, Y. Z. Li and Y. Cui, *Sci. Adv.*, 2011, **3**, e1701301.

View Article Online
DOI: 10.1039/D1EE03604A

31. L.L. Wang, S. Y. Fu, T. Zhao, J. Qian, N. Chen, L. Li, F. Wu, R. J. Chen, *J. Mater. Chem. A*, 2020, **8**, 1247.

32. F. Aqra and A. Ayyad, *Metall. Mater. Trans. A*, 2011, **42**, 2680-2684.

33. H. Okamoto, *J. Phase Equilibria. Diffus.*, 2012, **33**, 500.

34. J. Kasemchainan, S. Zekoll, D. S. Jolly, Z. Y. Ning, G. O., Hartley, J. Marrow and P. G. Bruce, *Nat. Mater.*, 2019, 18, 1105–1111.

35. T. Krauskopf, H. Hartmann, W. G. Zeier and J. Janek, *ACS Appl. Mater. Inter.*, 2019, **11**, 14463–14477.

36. X. Liu, J. Q. Huang, Q. Zhang and L. Q. Mai, *Adv. Mater.*, 2017, **29**, 1601759.

37. A. Manthiram, Y.Z. Fu, S.-H., Chung, C. X. Zu and Y. S. Su, Chem. Rev., 2014, 114, 11751-11787.

38. W. J. Xue, Z. Shi, L. M. Suo, C. Wang, Z. Q. Wang, H. Z. Wang, K. P. So, A. Maurano, D. W. Yu, Y. M. Chen, L. Qie, Z. Zhu, G. Y. Xu, J. Kong and J. Li, *Nat. Energy*, 2019, **4**, 374-382.

39. A. Jain, S. P. Ong, G. Hautier, W. Chen, W. D. Richards, S. Dacek, S. Cholia, D. Gunter, D. Skinner, G. Ceder and K. A. Persson, *APL Mater.*, 2013, **1**, 011002.

40. R. Nityananda, P. Hohenberg and W. Kohn, *Phys. Rev.*, 1964, **136**, B864.

41. W. Kohn and L. J. Sham, *Phys. Rev.*, 1965, **140**, A1133.

42. G. Kresse, *Phys. Rev. B.*, 1993, **47**, 558.

43. P. E. Blöchl, *Phys. Rev. B.*, 1994, **50**, 17953.

44. G. Kresse and J. Furthmüller, *Phys. Rev. B.*, 1996, **54**, 11169.

45. J. P. Perdew, K. Burke and M. Ernzerhof, *Phys. Rev. Lett.*, 1996, **77**, 3865.

View Article Online
DOI: 10.1039/D1EE03604A

46. S. Grimme, J. Antony, S. Ehrlich and H. Krieg, *J. Chem. Phys.*, 2010, **132**, 154104.

47. H. J. Monkhorst and J. D. Pack, *Phys. Rev. B.*, 1976, **13**, 5188.

48. K. Momma and F. Izumi., *J. Appl. Crystallogr.*, 2011, **44**, 1272–1276.

49. P. Canepa, J. A. Dawson, G. S. Gautam, J. M. Statham, S. C. Parker and M. S. Islam, *Chem. Mater.*, 2018, **30**, 3019–3027.

50. H. K. Tian, B. X. and Y. Qi, *J. Power Sources*, 2018, **392**, 79–86.

51. T. Thompson, S. Yu, L. Williams, R. D. Schmidt, R. G. Mendez, J. Wolfenstine, J. L. Allen, E. Kioupakis, D. J. Siegel and J. Sakamoto, *ACS Energy Lett.*, 2017, **2**, 462–468.